ELSEVIER

Journal of Nuclear Materials 266–269 (1999) 58–66

journal of nuclear materials

Erosion/redeposition analysis: status of modeling and code validation for semi-detached tokamak edge plasmas [1]

J.N. Brooks [a,*], D. Alman [b], G. Federici [c], D.N. Ruzic [b], D.G. Whyte [d]

[a] *Argonne National Laboratory, 9700 South Cass Avenue, Argonne, IL 60439, USA*
[b] *University of Illinois at Urbana/Champaign, 103 S. Goodwin Ave., Urbana, IL 61801, USA*
[c] *ITER Joint Work Site, Garching Co-centre, Boltzmannstrasse 2, 85748 Garching, Germany*
[d] *University of California at San Diego, La Jolla, CA 92093, USA*

Abstract

We are analyzing erosion and tritium codeposition for ITER, DIII-D, and other devices with a focus on carbon divertor and metallic wall sputtering, for detached and semi-detached edge plasmas. Carbon chemical-sputtering/hydrocarbon-transport is computed in detail using upgraded models for sputtering yields, species, and atomic and molecular processes. For the DIII-D analysis this includes proton impact and dissociative recombination for the full methane and higher hydrocarbon chains. Several mixed material (Si–C doping and Be/C) effects on erosion are examined. A semi-detached reactor plasma regime yields peak net wall erosion rates of ~1.0 (Be), ~0.3 (Fe), and ~0.01 (W) cm/burn-yr, and ~50 cm/burn-yr for a carbon divertor. Net carbon erosion is dominated by chemical sputtering in the ~1–3 eV detached plasma zone. Tritium codeposition in divertor-sputtered redeposited carbon is high (~10–20 g T/1000 s). Silicon and beryllium mixing tends to reduce carbon erosion. Initial hydrocarbon transport calculations for the DIII-D DiMES-73 detached plasma experiment show a broad spectrum of redeposited molecules with ~90% redeposition fraction.

Keywords: Carbon erosion; Erosion/redeposition; ITER; Tritium inventory

1. Introduction

Sputtering erosion/redeposition (E/R) of plasma facing components (PFCs) remains a critical issue for fusion reactor development. Key issues are: (1) net sputtering erosion rates and resulting divertor/limiter/wall lifetime, (2) codeposited tritium rates and locations, and (3) core plasma contamination. To analyze this subject we are using and improving coupled codes/models for sputtered particle yields, impurity transport, and sheath–particle interactions – these are used with inputs from plasma fluid and neutral edge codes. Refs. [1,2] discussed recent E/R calculations for a variety of plasma regimes, edge geometries, and coating materials. We are currently analyzing the performance of PFCs for detached and semi-detached edge plasma regimes. Such plasma regimes – identified by plasma fluid code studies and also found experimentally – may give reasonable surface heat loads ($\leqslant 5$ MW/m^2) and adequate helium removal. Unfortunately, when combined with carbon, there are exceptional difficulties in E/R modeling due to complex hydrocarbon transport and the lack of low-energy sputtering, reflection, and atomic and molecular process data. For example, for detached conditions about half of carbon chemical emission is in the form of non-methane hydrocarbons, unlike higher energies where methane dominates. To improve the models we are conducting code validation using carbon erosion data from the DIII-D–DiMES probe and have begun analyzing other experiments (JET, PISCES). As a major modeling upgrade we have developed rate coefficient estimates for chemically sputtered hydrocarbons and fragments, for detached conditions, and have implemented the full hydrocarbon transport in the codes. This paper will present the status of these studies.

* Corresponding author. Tel.: +1-630 252 4830; fax: +1-630 252 5287; e-mail: brooks@anl.gov.

[1] US work was supported by the US Department of Energy, Office of Fusion Energy.

0022-3115/99/$ – see front matter
PII: S0022-3115(98)00822-8

1.1. Tokamak reactor analysis

The ITER PFC design [3,4] illustrates numerous erosion/redeposition issues of generic interest to fusion development. ITER is a low duty-factor experimental reactor in which frequent expected plasma disruptions dictate the choice of surface material. The ITER boundary is shown in Fig. 1. Carbon is chosen as the main divertor target material due to its good disruption performance. The first wall is beryllium coated. A portion of the divertor and the 'baffle' regions are tungsten coated. For this study we primarily use the typical ITER 'Case 98', 0.7% neon, semi-detached solution [5]. As described in Refs. [1,2] we apply the DEGAS$^+$ code [6] to the basic 2-D solution to give high spatial resolution neutral flux information needed for the erosion analysis. Plasma parameters and fluxes along the outer divertor plate for this solution are shown in Fig. 2. There is a rough division between an attached plasma zone of width ~70 cm with temperatures ~3–30 eV, and a ~20 cm detached zone of $\leqslant 3$ eV with high density near the separatrix. Due to the high density, particle fluxes – including the non-thermal ('fast') molecular flux – are high in the detached portion. Plasma parameters along the wall (not shown) are of order $T_i \approx 30$ eV, $N_i \approx \times 10^{17}$ m^{-3}.

2. First wall erosion

2.1. Method

The tokamak first wall will be eroded by three classes of particles: (1) D–T ions diffusing to the wall, (2) D–T neutrals arising from ion recycling (at both divertor and wall), and (3) D–T neutrals arising from gas puffing. Wall erosion by ions is highly dependent on uncertain wall boundary conditions (e.g. wall sheath, if any) and is only crudely estimated for this study. Wall erosion by neutrals is computed in detail. To compute wall neutral flux from ion recycling a DEGAS$^+$ simulation was performed on the ITER Case 98 target plasma by launching recycling atoms/molecules from the divertor (with ion source shown in Fig. 2) and the wall. A wall ion flux of N_i/d is used where N_i is the density at the computational boundary (3 cm from the wall), and $d = 0.03$ s/m, corresponding to diffusive estimates [7]. For gas-puffing, puffing is done from one toroidal and poloidal location – near the outer midplane – at a distance of 8 cm from the plasma boundary and the results scaled for the ~1.5 m^2 area of the gas puff design. All neutral–neutral and neutral–ion elastic collisions are included which spreads the incoming gas cloud. Charge exchange is the dominant mechanism once the ITER plasma boundary is reached. The average energy of D/T atoms returning from the plasma and striking the gas puffing point ranges from 60 to 70 eV over a poloidal extent of 30 cm. Their energy quickly rises to the 200–300 eV range at further poloidal distances from the injection point, but the flux is down by one or more orders of magnitude. The returned molecular flux is more peaked and has an average energy of about 4 eV – in equilibrium with the local ion flow velocity.

Wall erosion is computed using the DEGAS$^+$ neutral flux results as input to the WBC$^+$ Monte Carlo code to compute sputtering and impurity transport. The latter is an extension of WBC [8] which traces the transport of

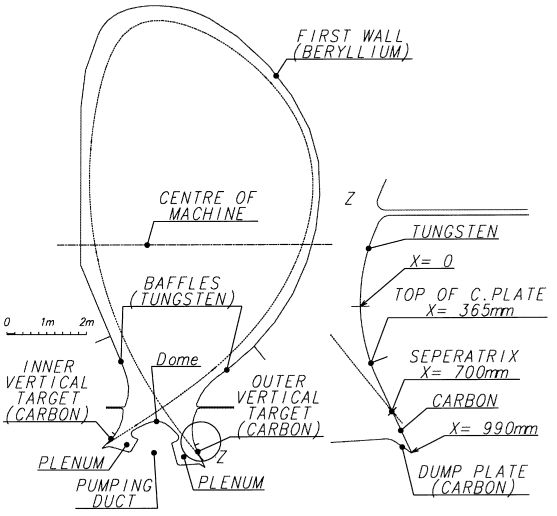

Fig. 1. ITER plasma facing surfaces geometry including detail of outer divertor target.

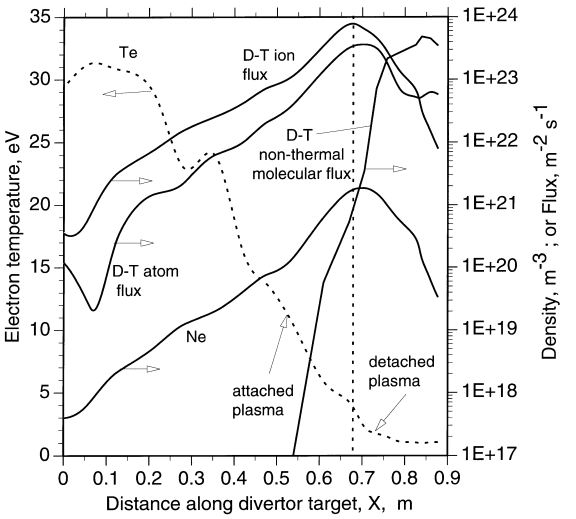

Fig. 2. Plasma temperature, density, and particle fluxes along the ITER outer divertor target for a semi-detached edge plasma.

sputtered material in and around the scrapeoff layer. Three materials are examined – beryllium (ITER reference), iron representing a bare wall, and tungsten coating.

2.2. Results

Gas puffing is the dominant source of peak wall erosion whereas total erosion is due about equally to ion impingement, gas puffing and ion recycling. In general, wall erosion is lower for the semi-detached regime than for a fully detached regime [2], in part because there is less 'transparency' of divertor recycled neutrals to the wall regions. Gas-puffing erosion results are shown in Fig. 3. These profiles are highly peaked. The beryllium peak, at ~1 cm/burn-yr is acceptable for low duty-factor operation only, e.g. ITER. The iron (bare wall) results are disappointing in not being much better than beryllium. This is due to the high energy D–T neutrals arising from charge exchange with the hot plasma edge. Tungsten erosion is two orders of magnitude lower.

The WBC^+ results for wall-sputtered beryllium atoms show that: 55% goes to the core plasma, 38% goes the divertor plates, and 7% goes elsewhere (dome and plenum). None return to the wall but this is partly because diffusion is not fully modeled. Wall material entering the core plasma will subsequently flow primarily to the divertor. We conclude, therefore, that wall sputtered beryllium will be mostly deposited on the divertor plates. (SOL transport of the other materials has not been computed.) Subsequent sputtering of the divertor will tend to transport beryllium to the bottom of the plates and to the plenum region.

The tritium codeposition in wall-sputtered redeposited beryllium is estimated based on a total sputtered beryllium current of $\sim 2 \times 10^{21}$ s^{-1}, about half of which is deposited in high surface temperature (>500°C) divertor target regions with little or no codeposition, and about half of which builds up in lower temperature areas (bottom of divertor targets and plenum region). Using coldest deposition surface temperatures for the latter of ~230°C we can estimate approximate worst-case codeposition rates. These are ~0.1 g T/1000 s using linearly-scaled low-oxygen-content Tritium Plasma Experiment (TPE) trapping data [9] (H/Be = 0.05) or ~0.6 g T/1000 s using 'carbon-corrected' Mayer et al. data [10] (H/Be = 0.23). In either case the wall-derived T/Be codeposition is much less than codeposition from carbon divertor sputtering.

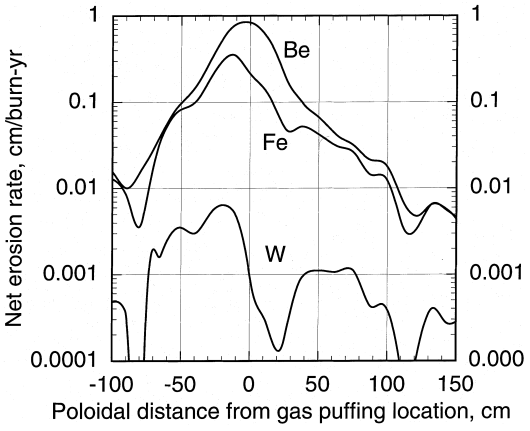

Fig. 3. Erosion of ITER first wall due to gas-puffing charge exchange flux.

3. Divertor erosion

3.1. Method

The coupled REDEP [11]/WBC impurity transport codes are used to compute carbon physical and chemical sputtering, carbon/hydrocarbon transport, and redeposition/codeposition for the inner and outer vertical divertor target plates. Alternative materials are also examined. For simplicity in the analysis, the entire target regions are assumed to be carbon coated – the small tungsten coated target region has only a small effect on overall results. Carbon sputtering is by D, T ions atoms and fast molecules, He ions, and self-ions. Codeposition is computed based on surface temperature profiles and H/C temperature-dependent trapping ratios [12]. For the ITER computations methane-only chemical emission was employed as the new model (Section 5) was not yet available. Carbon chemical sputtering yields for detached conditions (D, T ~5–15 eV impingement energy, ~500–800 K surface temperatures) are uncertain. This work uses a compilation of best-estimate yields, assembled by an ITER expert group, and known as the 'subcommittee' model [4]. These model yields, are in the range ~1–2%. Finally, a nominal reference value of 0.001 is used for the highly uncertain fast-molecule chemical sputtering yield.

3.2. Results

Figs. 4 and 5 show gross and net erosion of the outer plate for physical sputtering and chemical sputtering, respectively. These are shown separately to illustrate trends. The inner plate results (not-shown) are similar. For physical sputtering, carbon atoms are ionized primarily near the surface due to the high electron temperature and redeposit primarily on the target. Only a small fraction (1.5×10^{-4}) leave the near-surface region, implying a low potential for core plasma contamination. For chemical sputtering the codes predict nearly 100% redeposition on the attached portion of the plates, and about ~80–90% redeposition on the detached portion.

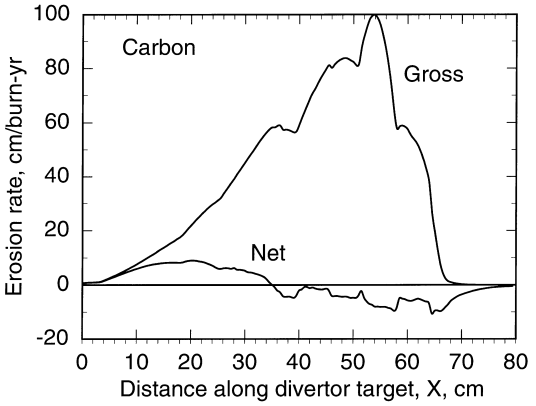

Fig. 4. Carbon divertor erosion due to physical sputtering only.

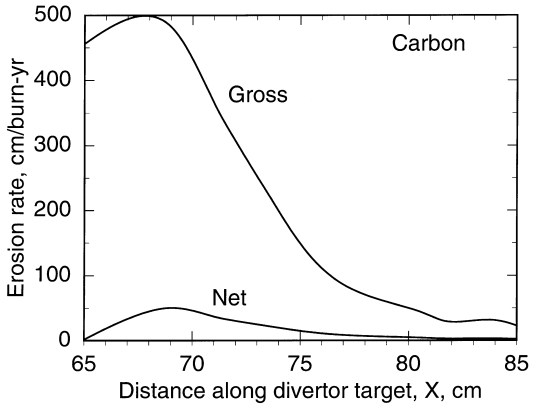

Fig. 5. Carbon divertor erosion due to chemical sputtering only.

Thus, the detached portion is critical to net erosion and codeposition. The reason for the ~10–20% carbon loss is non-ionization (too-cold plasma) and escape of a fraction of the end-chain carbon atoms formed by the hydrocarbon transport process – as discussed further in Ref. [1].

The combined (physical and chemical) erosion analysis shows that carbon builds up mostly on the bottom of the target and dump plates (~75%), and in the plenum region (~25%). These surfaces are relatively cold (~230°C) which contributes to high codeposition.

Table 1 summarizes peak net erosion rates and total tritium codeposition rates for the reference divertor case and various other cases. The codeposition rate for the reference conditions is 14 g T for the 1000 s ITER pulse. This varies with assumed fast-molecule yield (Cases 2, 3), but less so than for a fully detached regime [1] due to less fast-molecule generation. Physical sputtering contributes about 20% to codeposition. Be/C mixing (Case 5), to be described, reduces codeposition by ~25%. A beryllium coated divertor, like carbon, shows high net erosion (due to physical sputtering) but much less codeposition. Tungsten shows low erosion (precise amount needing more detailed analysis) and essentially no codeposition. Finally, for a somewhat different plasma solution [13] (''Case 133-shallow detached'' involving a wider detached zone), the results are qualitatively similar with tritium codeposition, about 20% higher. In contrast to codeposition, an integral quantity, peak erosion depends on numerous profile effects, and is highest for the reference case.

4. Mixed material analysis

We analyzed divertor erosion for two cases of mixed materials: (1) silicon doped carbon fiber composite material, ''NS-31'' nominally containing 8% Si which has been proposed as an alternative divertor coating in order to reduce chemical sputtering [14], and (2) wall-sputtered beryllium effect on a carbon divertor. Both analyses are for the Case 98 plasma solution. The model used for

Table 1
REDEP/WBC analysis of divertor erosion/codeposition, ITER semi-detached edge plasma

	Case	Peak net erosion rate (cm/burn-yr)	Tritium codeposition rate[a] (g T/1000 s pulse)
1.	Reference[b]	49	14
2.	No fast-molecule chemical sputtering	49	13
3.	$Y_{mol} = 0.01$	49	24
4.	No chemical sputtering (physical sputtering only)	9	2
5.	Carbon erosion reduced due to beryllium (from wall) mixing	47	11
6.	Beryllium divertor coating[c]	30	2
7.	Tungsten divertor coating	<0.1	~0
8.	'Shallow detached' plasma [13]	23	17

[a]Total (inner + outer divertor) resulting from vertical target sputtering.
[b]Reference: carbon coating, Case 98-semi-detached plasma, physical and chemical sputtering, non-thermal D–T molecule sputtering yield $Y_{mol} = 0.001$.
[c]With TPE H/Be trapping ratio data [9].

time-evolution of surface composition is based on simple particle counting and perfect mixing in an interaction zone of fixed depth (10 nm). For Be/C the chemical yield is assumed to be reduced based linearly on the Be/C fraction [15]. The beryllium ion flux to the divertor is computed based on the total wall sputtering and assuming that the plasma-transported Be flux is everywhere proportional to the D–T ion flux. Details of the model will be published elsewhere.

For the NS-31 material both net erosion and corresponding growth rates at equilibrium surface conditions (reached at ~1 minute) are somewhat lower (~25%) than for pure carbon. This is due to the more favorable redeposition characteristics of the silicon compared to carbon.

For Be/C we find low beryllium surface fractions on the attached portions of the plates due to very low Be/D–T and Be/C flux ratios, and also high physical sputtering. Beryllium does build up on the detached portion where the physical sputtering is very low or zero (cold plasma). The surface fraction of beryllium varies from ~0 on the attached portions, to ~4% at the separatrix, and to 100% at the bottom. Fig. 6 shows the net erosion rate of Be-mixed carbon compared to pure carbon in the detached portion along the outer plate. The beryllium mixture/overlayer suppresses carbon erosion in this region leading to the ~25% reduction in tritium codeposition (Table 1). Since this is a significant effect, a more sophisticated analysis, incorporating, for example, nonlinear mixing effects, is warranted.

5. DIII–D73 experiment and improved hydrocarbon transport modeling

The D-73 detached plasma experiment was conducted in January 1998, and is described in Ref. [16]. This involved impingement of ~5–10 eV D^+ ($T_e \approx 1$–2 eV) on a carbon DiMES (Divertor Material Evaluation Studies) probe in the DIII-D lower divertor with extensive plasma diagnostic data and post-exposure probe erosion measurements obtained. We have begun analysis of this experiment using WBC. A major code update is the addition of essentially the full sputtered hydrocarbon spectrum. We use hydrocarbon launch fractions from UTIAS data [17]. For 10 eV D these values, in terms of 'carbon fractions' are: CH_4 (0.42), C_2H_2 (0.036), C_2H_4 (0.24), C_2H_6 (0.11), C_3H_6 (0.16), C_3H_8 (0.035). We treat all of these except propane (C_3H_8), this being only a ~4% effect as shown. (C_2H_2 must be included because it is formed by higher hydrocarbon breakup processes.)

Appendix A describes the hydrocarbon chemistry model. This was implemented in WBC along the lines described in Ref. [18] with various modifications to the Monte Carlo techniques, e.g. to follow multi-particle breakup. No particle reflection is included now pending development of a complete reflection model. Such a reflection can be highly important to overall redeposition fractions [1–18]. Preliminary D-73 analysis is made for transport in the near-surface region (0–5 cm) where the plasma parameters were approximately constant.

For the D-73 analysis particles are launched per the above carbon fractions. A particle history terminates upon hitting the surface or leaving the near-surface region. Fig. 7 shows the code results for 10 000 particles launched. The redeposition spectrum is complex, with overall carbon redeposition fraction of 88%, again not including reflection effects. Most non-redeposited material is in the form of ~5–10 eV (end-stage product) carbon atoms heading away from the surface. This and related code output will be used to check against erosion, photon emission, and other data [16]. The analysis will be extended to include the attached/detached transition region.

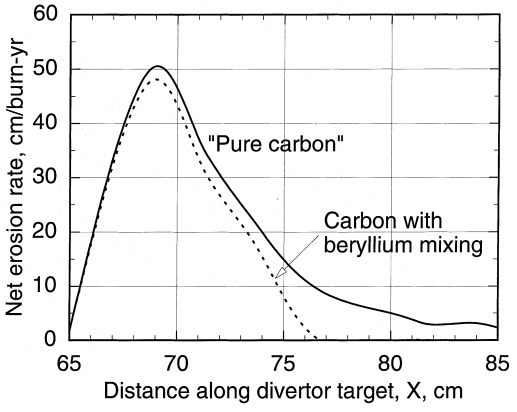

Fig. 6. Erosion of divertor with pure carbon and beryllium-mixed carbon.

6. Conclusions

This work has analyzed erosion/redeposition/codeposition of carbon, beryllium, and tungsten, divertor and wall materials, for detached/semi-detached regimes of current interest to reactor designs and major operating tokamaks. For ITER the predicted net erosion rates are marginally acceptable. Tritium codeposition in carbon is conditionally acceptable for ITER, based on demonstration of suitable cleanup techniques, but not for future high-duty factor devices. Likewise, a beryllium wall should work for ITER but does not extrapolate to future reactors. Tungsten performs well from the standpoints analyzed. Based on the approximate analysis used here mixed material effects are likely to be significant and, therefore, need further detailed analysis.

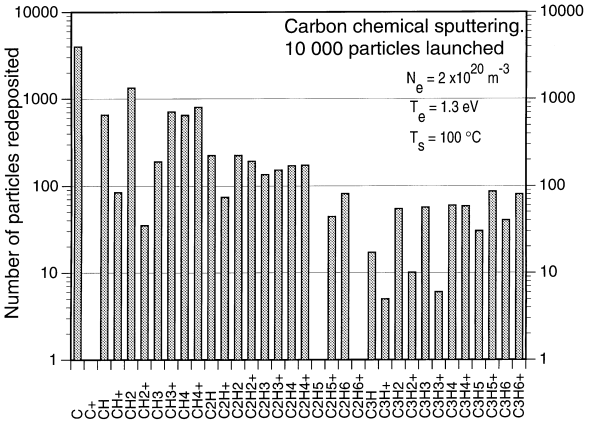

Fig. 7. Carbon/hydrocarbon redeposited species mix from WBC code analysis of DIII–D/D73 detached plasma experiment.

Due to numerous model uncertainties, not the least of which are the plasma solutions themselves, the present results should properly be viewed as identifying trends, and not used for precise predictive purposes. This contrasts to fully attached regimes where we have at least partial validation of the codes. Key uncertainties for carbon include chemical sputtering yield of fast molecules and low energy particles in general, flux effects on sputtering, and atomic and molecular process rates.

A major update to the erosion/redeposition codes is the full hydrocarbon reaction set for chemical sputtering. This should be useful for full analysis of carbon erosion in DIII-D and other devices.

Appendix A. Hydrocarbon plasma chemistry model

Four categories of reactions were investigated: electron impact ionization (including dissociative ionization), electron impact dissociation, proton impact ionization, and dissociative recombination. For the 1–3 eV regime that we are interested in, the latter two categories are the most important and will be discussed here. The complete model will be published elsewhere [19].

A.1. Proton impact ionization

Gioumousis and Stevenson [20] found that the rate constant for an ion–molecule collision process is related to the cross section, $\bar{q}$ by

$$k = \bar{q}v, \tag{A.1}$$

where v is the velocity of the ion. If a reaction is assumed to take place at every collision, the cross section is given by

$$\bar{q} = \frac{2\pi}{v}\left(\frac{e^2\alpha}{M_r}\right)^{1/2}, \tag{A.2}$$

where e is the ion charge, α is the molecular polarizability of the reactant molecule, and M_r is the reduced mass of the reacting system. By substituting this expression for the cross section into Eq. (A.1) we get a useful formula for calculating reaction rates for ion–molecule collisions.

$$k = \frac{2\pi}{v}\left(\frac{e^2\alpha}{M_r}\right)^{1/2}. \tag{A.3}$$

Unfortunately, molecular polarizability data are not often available. To make matters worse, the relationship between polarizability and reaction rates means that most molecules that have unknown reaction rates also have unknown polarizabilities. However, the unknown molecular polarizabilities can be calculated from the molar refraction according to the Lorentz–Lorenz relation

$$\alpha = \frac{3}{4\pi N_A}R, \tag{A.4}$$

where N_A is Avogadro's number, and R is the molar refraction. For many compounds, the molar refraction is approximately proportional to the number of each type of atom present. A least squares fit was done using known values, and the resulting relationship is

$$R = 3.939(\#\text{ C atoms}) + 0.5452(\#\text{ H atoms}). \tag{A.5}$$

These values can be used in Eq. (A.4) to calculate polarizabilities, which can in turn be used in Eq. (A.3) to calculate the total proton impact reaction rate for every hydrocarbon molecule of interest at thermal energy. These are shown in Table 2. There is very little energy dependence from thermal energies up to a few eV, so that the rate constants at 300 K are acceptable for our model and have been investigated here.

The branching ratio, however, does not remain constant up to a few eV. At thermal energies where the experimental measurements in Table 2 were taken, one

Table 2
Proton impact ionization reaction rate coefficients

Reactants		Products	Derived total (cm^3/s)	Experimental value (cm^3/s)	Refs.
$H^+ + CH_4$	→	$0.5\ CH_4^+ + H$	4.15×10^{-9}	3.8×10^{-9}	[22]
		$0.5\ CH_3^+ + H_2$		4.15×10^{-9}	[22]
$H^+ + CH_3$	→	$0.5\ CH_3^+ + H$	3.6×10^{-9}	–	
		$0.5\ CH_2^+ + H_2$			
$H^+ + CH_2$	→	$0.5\ CH_2^+ + H$	3.4×10^{-9}	–	
		$0.5\ CH^+ + H_2$			
$H^+ + CH$	→	$1.0\ CH^+ + H$	3.2×10^{-9}	–	
$H^+ + C_2H_6$	→	$0.33\ C_2H_5^+ + H_2$	3.9×10^{-9}	3.9×10^{-9}	[22,23]
		$0.33\ C_2H_4^+ + H_2 + H$			
		$0.33\ C_2H_3^+ + H_2 + H_2$			
$H^+ + C_2H_5$	→	$0.33\ C_2H_5^+ + H$	4.9×10^{-9}	–	
		$0.33\ C_2H_4^+ + H_2$			
		$0.33\ C_2H_3^+ + H_2 + H$			
$H^+ + C_2H_4$	→	$0.33\ C_2H_4^+ + H$	5.0×10^{-9}	5.0×10^{-9}	[24]
		$0.33\ C_2H_3^+ + H_2$			
		$0.33\ C_2H_2^+ + H_2 + H$			
$H^+ + C_2H_3$	→	$0.33\ C_2H_3^+ + H$	4.6×10^{-9}	–	
		$0.33\ C_2H_2^+ + H_2$			
		$0.33\ C_2H^+ + H_2 + H$			
$H^+ + C_2H_2$	→	$0.5\ C_2H_2^+ + H$	6.3×10^{-9}	6.3×10^{-9}	[24]
		$0.5\ C_2H^+ + H_2$			
$H^+ + C_2H$	→	$1.00\ C_2H^+ + H$	4.4×10^{-9}	–	
$H^+ + C_3H_6$	→	$0.33\ C_3H_6^+ + H$	5.8×10^{-9}	–	
		$0.33\ C_3H_5^+ + H_2$			
		$0.33\ C_3H_4^+ + H_2 + H$			
$H^+ + C_3H_5$	→	$0.33\ C_3H_5^+ + H$	5.7×10^{-9}	–	
		$0.33\ C_3H_4^+ + H_2$			
		$0.33\ C_3H_3^+ + H_2 + H$			
$H^+ + C_3H_4$	→	$0.33\ C_3H_4^+ + H$	5.9×10^{-9}	–	
		$0.33\ C_3H_3^+ + H_2$			
		$0.33\ C_3H_2^+ + H_2 + H$			
$H^+ + C_3H_3$	→	$0.33\ C_3H_3^+ + H$	5.5×10^{-9}	–	
		$0.33\ C_3H_2^+ + H_2$			
		$0.33\ C_3H^+ + H_2 + H$			
$H^+ + C_3H_2$	→	$0.5\ C_3H_2^+ + H$	5.4×10^{-9}	–	
		$0.5\ C_3H^+ + H_2$			
$H^+ + C_3H$	→	$1.0\ C_3H^+ + H$	5.2×10^{-9}	–	

channel tends to dominate over the others. However, some temperature dependent results indicate that the product distribution becomes more evenly distributed as temperature increases [21]. At the temperatures that we are interested in (~1–3 eV), we have assumed that all reactions produce an even distribution of products.

A.2. Dissociative recombination

The rate coefficient for dissociative recombination is known to be inversely proportional to temperature. The model used for these reactions is

$$\langle \sigma v \rangle = \frac{A}{T^B}, \tag{A.6}$$

where A and B are parameters to be determined. The reaction rate as a function of temperature is known for the methane family [25]. In these lighter hydrocarbons, there is a noticeable bend in the $\langle \sigma v \rangle$ vs. T plot, so the reaction rate has been split up into two sections, each with their own A and B, covering the temperature ranges $T < 1$ and $T > 1$ eV. For the heavier ions, the rate can be approximated by just one function for all energies. Of the 12 heavier hydrocarbons of importance, there are values of the reaction rate at one energy (usually 300 K) in the literature for six of them. The energy dependence was known for several of these ions to be $B = -1/2$ [24]. Using this energy dependence, together with the one data point, allows us to solve for the remaining parameter, A, for six of the ions.

The remaining six hydrocarbons present more of a challenge. Bates had proposed that the dissociative recombination rate is proportional to the number of bonds

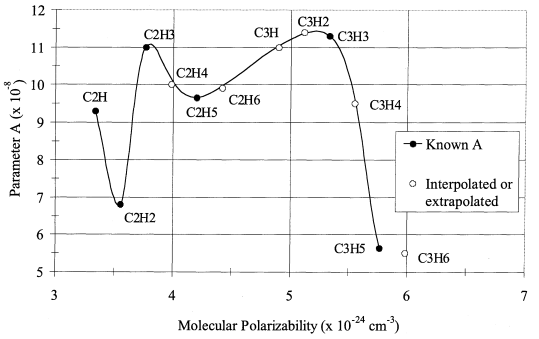

Fig. 8. Parameter A vs. polarizability.

that can be broken. There is some disagreement about whether this is true [26], and since the reaction rates that we know so far do not seem to follow this type of a trend, another method of estimation must be employed. If we assume that the rate of dissociative recombination again depends on the polarizability of the ion and we use the same value of $B = -1/2$, then it becomes rather easy to find these remaining reaction rates. A graph was constructed of the known values of the parameter A vs. molecular polarizability of the corresponding molecule. This is shown in Fig. 8. The value of A is found for five of the remaining hydrocarbons by interpolating from this graph, and by extrapolation for the other.

The branching ratios for the methane family are known or estimated [25]. The data available on branching ratios for some of the heavier hydrocarbons indicate that the product distributions are split evenly among the possible channels [24]. In our model, we use an even branching ratio for the dissociative recombination of these heavier molecules. The reaction rates are summarized in Table 3.

Table 3
Dissociative recombination reaction rate coefficients

Reactants		Products	Derived total (cm^3/s)		Experimental value (cm^3/s)	Ref.
$e^- + CH_4^+$	$\rightarrow$	0.25 CH_3 + H	$5.4 \times 10^{-8} T^{-0.084}$	$T <$ eV	3.8×10^{-9} at 0.0257 eV	[25]
		0.75 CH_2 + H_2	$5.4 \times 10^{-8} T^{-1.05}$	$T > 1$ eV	4.5×10^{-9} at 0.0259 eV	
$e^- + CH_3^+$	$\rightarrow$	1.00 CH_2 + H	$6.8 \times 10^{-8} T^{-0.770}$	$T < 1$ eV	–	[25]
			$6.8 \times 10^{-8} T^{-0.979}$	$T > 1$ eV		
$e^- + CH_2^+$	$\rightarrow$	1.00 CH + H	$1.0 \times 10^{-7} T^{-0.544}$	$T < 1$ eV	–	[25]
			$1.0 \times 10^{-7} T^{-1.21}$	$T > 1$ eV		
$e^- + CH^+$	$\rightarrow$	1.00 C + H	$7.0 \times 10^{-8} T^{-0.553}$	$T < 1$ eV	–	[25]
			$7.0 \times 10^{-8} T^{-1.18}$	$T > 1$ eV		
$e^- + C_2H_6^+$	$\rightarrow$	0.50 C_2H_5 + H	$9.9 \times 10^{-8} T^{-0.50}$		–	[24]
		0.50 C_2H_4 + H_2				
$e^- + C_2H_5^+$	$\rightarrow$	0.50 C_2H_4 + H	$9.65 \times 10^{-8} T^{-0.50}$		6.0×10^{-7} at 0.0259 eV	[27]
		0.50 C_2H_3 + H_2				
$e^- + C_2H_4^+$	$\rightarrow$	0.50 C_2H_3 + H	$1.00 \times 10^{-7} T^{-0.50}$		–	
		0.50 C_2H_2 + H_2				
$e^- + C_2H_3^+$	$\rightarrow$	0.50 C_2H_2 + H	$1.10 \times 10^{-7} T^{-0.50}$		1.6×10^{-6} at 0.00863 eV	[28]
		0.50 C_2H + H_2			4.5×10^{-7} at 0.0259 eV	[27]
$e^- + C_2H_2^+$	$\rightarrow$	0.33 C_2H + H	$6.81 \times 10^{-8} T^{-0.50}$		1×10^{-6} at 0.00863 eV	[28]
		0.33 CH + CH			2.7×10^{-7} at 0.0259 eV	[27]
		0.33 C + C + H + H				
$e^- + C_2H^+$	$\rightarrow$	0.50 C + C + H	$9.28 \times 10^{-8} T^{-0.50}$		1×10^{-6} at 0.00863 eV	[28]
		0.50 CH + C				
$e^- + C_3H_6^+$	$\rightarrow$	0.50 C_3H_5 + H	$5.50 \times 10^{-8} T^{-0.50}$		–	
		0.50 C_3H_4 + H_2				
$e^- + C_3H_5^+$	$\rightarrow$	0.50 C_3H_4 + H	$5.63 \times 10^{-8} T^{-0.50}$		3.5×10^{-7} at 0.0259 eV	[27]
		0.50 C_3H_3 + H_2				
$e^- + C_3H_4^+$	$\rightarrow$	0.50 C_3H_3 + H	$1.10 \times 10^{-7} T^{-0.50}$		–	
		0.50 C_3H_2 + H_2				
$e^- + C_3H_3^+$	$\rightarrow$	0.50 C_3H_2 + H	$1.10 \times 10^{-7} T^{-0.50}$		7.0×10^{-7} at 0.0259 eV	[26]
		0.50 C_3H + H_2			7.0×10^{-7} at 0.0259 eV	[27]
$e^- + C_3H_2^+$	$\rightarrow$	0.50 C_2H + CH	$1.10 \times 10^{-7} T^{-0.50}$		–	
		0.50 C_3H + H				
$e^- + C_3H^+$	$\rightarrow$	0.33 CH + C + C	$1.10 \times 10^{-7} T^{-0.50}$		–	
		0.33 C_2H + C				
		0.33 C + C + C + H				

References

[1] J.N. Brooks, R. Causey, G. Federici, D.N. Ruzic, J. Nucl. Mater. 241–243 (1997) 294.
[2] J.N. Brooks, D.N. Ruzic, D.B. Hayden, Fusion Eng. Design 37 (1997) 455.
[3] K.J. Dietz et al., Fusion Eng. Design 27 (1995) 96.
[4] G. Federici et al., these Proceedings.
[5] A. Kukushkin et al., IAEA-CN-64/FP-27, 1996.
[6] D.N. Ruzic, Phys. Fluids B 5 (1993) 3140.
[7] H. Pacher, A. Kukushkin, ITER JCT, 1997, personal communication.
[8] J.N. Brooks, Phys. Fluids 8 (1990) 1858.
[9] R.A. Causey, D. Walsh, J. Nucl. Mater. 254 (1998) 84.
[10] M. Mayer et al., J. Nucl. Mater. 230 (1996) 67.
[11] J.N. Brooks, Nucl. Tech. Fusion 4 (1983) 33.
[12] B. Doyle et al., J. Nucl. Mater. 103/104 (1981) 513.
[13] A. S. Kukushkin et al., Proceedings of EPS-97, ECA 21A (Part III) (1997) 1001.
[14] M. Balden, Max-Planck-Institut für Plasmaphysik, Report IPP9/112NS-31.
[15] J. Roth IPP-Garching, T. Haasz UTIAS, 1997, personal communication .
[16] D.G. Whyte et al., these Proceedings.
[17] B.V. Mech, A.A. Haasz, J.W. Davis, J. Nucl. Mater. 255 (1998) 153; J. Nucl. Mater. 241–243 (1997) 1147.
[18] J.N. Brooks, ANL/FPP/TM-259, 1992.
[19] D.A. Alman, M.S. Thesis, University of Illinois, to be published.
[20] E.W. McDaniel, V. Cermák, A. Dalgarno, E.E. Ferguson, L. Friedman, Ion–Molecule Reactions, Wiley–Interscience, New York, 1970, pp. 293–296.
[21] S. Dheandhanoo, R. Johnsen, M.A. Biondi, Planet. Space Sci. 32 (1984) 1301.
[22] V.G. Anicich, W.T. Huntress, Jr., Astrophys. J. Supp. Series 62 (1986) 553.
[23] G.I. Mackay, H.I. Schiff, D.K. Bohme, Can. J. Chem. 59 (1981) 1771.
[24] D. Schultz, ORNL, 1997, personal communication.
[25] A.B. Ehrhardt, W.D. Langer, PPPL-2477, 1987.
[26] H. Abouelaziz, J.C. Gomet, D. Pasquerault, B.R. Rowe, J.B.A. Mitchell, J. Chem. Phys. 99 (1993) 237.
[27] J.B.A. Mitchell, C. Rebrion-Rowe, Int. Rev. Phys. Chem. 16 (1997) 201.
[28] P.M. Mul, J.W. McGowan, Astrophys. J. 237 (1980) 749.